Carbon 134 (2018) 345–353

Contents lists available at ScienceDirect

Carbon

journal homepage: www.elsevier.com/locate/carbon

3D self-assembly synthesis of hierarchical porous carbon from petroleum asphalt for supercapacitors

Lei Pan, Yixian Wang, Han Hu, Xinxin Li, Jialiang Liu, Lu Guan, Wei Tian, Xiaobo Wang, Yanpeng Li, Mingbo Wu*

State Key Laboratory of Heavy Oil Processing, College of Chemical Engineering, China University of Petroleum (East China), Qingdao 266580, PR China

ARTICLE INFO

Article history:
Received 3 February 2018
Received in revised form
2 April 2018
Accepted 3 April 2018
Available online 5 April 2018

Keywords:
Self-assembly
Petroleum asphalt
Hierarchical porous carbon
Supercapacitors

ABSTRACT

A facile and scalable three-dimensional self-assembly template synthesis of hierarchical porous carbon method is developed. During the synthesis, KCl with face-centered cubic crystal is adopted to guide the growth of 3D porous carbon networks. Remarkably, the intimate interconnect porous feature not only significantly speeds up the electron transfer via shortened ion diffusion distance, but also exposes the electrochemically accessible active sites through ultrahigh surface area up to 3581 $m^2 g^{-1}$. As electrodes for button type supercapacitors, the HPC electrode shows a high capacitance of 277 $F g^{-1}$ at 0.05 $A g^{-1}$, superior rate performance of 194 $F g^{-1}$ at 20 $A g^{-1}$ and excellent cyclic stability of 95.1% after 10000 charge and discharge cycles at 2 $A g^{-1}$ in 6 M KOH electrolyte. Furthermore, the HPC based symmetric supercapacitors possess high specific energy density of 14.2 Wh kg^{-1} at a power density of 445 W kg^{-1} operated in the wide voltage range of 1.8 V in the Na_2SO_4 electrolyte. This work opens up a facile way for efficient and scaled-up production of low-cost electrode materials with high performance for other energy storage devices.

1. Introduction

The increasing energy demand and environmental sustainability have prompted worldwide efforts to develop low cost, environmentally friendly and high power energy storage devices [1,2]. Among these devices, supercapacitor as a traditional energy storage device has attracted much attention because of their intriguing characteristics, including the fast charge-discharge, high power density and excellent stability [3,4]. As we all know, the electrochemical performance of supercapacitors mainly depends on the electrode material [5]. Recently, transition-metal compounds hold great promise for supercapacitors due to their higher capacitance performances [6], but the surface faradaic redox reactions usually involve a complex multi-ion and multi-electron transfer process, which is greatly limited by unfavorable reaction kinetics, thus leading to the inferior rate capability and low power density [7]. How to fortify the energy density without sacrificing power density deserves further studies. Carbon-based materials have attracted great attention ascribed to their comprehensive merits including stable chemical properties and excellent power densities [8–11]. One barrier for hindering industrialization of supercapacitors is the inferior energy density. The energy density is proportional to the square of the voltage window, thus the efficient way to enhance the energy density is increasing voltage window. Generally, organic and ionic liquid electrolytes possess higher voltage window, nevertheless, most of them are expensive and unstable, which hinder their wide applications. Aqueous electrolytes have received wide attention due to their affordable and excellent stability (such as Li_2SO_4, K_2SO_4 and Na_2SO_4). Among them, Na_2SO_4 occupies an important position due to their high voltage window (even higher than 2 V).

Currently, great efforts have been devoted to designing and optimizing various porous materials for improving the energy storage capabilities. The template method has been widely employed [12,13], during which various soft templates, hard templates and dual templates have been employed. He et al. reported the preparation of 3D interconnected graphene nanocapsules from coal tar pitch by a nano ZnO template coupled with in-situ KOH activation strategy and the resultants showed excellent cycle stability [14]. Hu et al. used MgO as the template and benzene as the carbon precursor to prepare carbon nanocages by capillarity synthesis and the products displayed ultrahigh volumetric

* Corresponding author.
E-mail address: wumb@upc.edu.cn (M. Wu).

https://doi.org/10.1016/j.carbon.2018.04.008
0008-6223/

performance [15]. In summary, different porous carbons keep various morphologies by inheriting from the metal oxide precursor [16]. Nevertheless, the synthetic process should be scalable for industrial manufacturing and the use of metal oxide as template possesses many weaknesses, including the water insoluble and chemical inert features. Thus, causticity acid (HCl or HF) must be used to remove templates [17]. Furthermore, the solid template displays a less interaction during the carbonization process, it is very valuable to explore new preparation technology of hierarchical porous carbon from cheap materials for realizing high value-added utilization [18]. By comparison with conventional metal oxide, metal chloride templates have many physical advantages. Firstly, salt reserves are abundant and can be easily obtained; secondly, salts can be facilely removed using deionized water rather than chemical etching; thirdly, metal chloride salts are environmentally friendly and easily recovered [12,19–22]. Additionally, these salts have lower melting point compared with metal oxides. During the carbonation process, solid or liquid template could efficiently modulate porous carbon morphologies and pore sizes [23,24]. Among the metal chlorides, potassium chloride with relatively low melting point (770 °C) and cubic crystal feature easily recrystallizes under heating process [25].

Petroleum asphalt as a byproduct of crude distillation is affluent in China and it contains a large amount of polycyclic aromatic hydrocarbons that are easy to be polymerized and aromatized to form thin carbon sheets or cages during the heat treatment process [26]. These thin carbon sheets are fine materials that can be applied to gas absorption, catalyst support and energy storage, etc [17,27,28]. Therefore, it is possible to develop an environmentally friendly method to fulfill high value-added utilization of petroleum asphalt for supercapacitors.

Herein, nitrogen doped hierarchical porous carbons from petroleum asphalt were successfully synthesized using in situ KOH activation coupled with potassium chloride as the solvent and self-assembly templates. In the carbonization process, KCl melts and self-assembly forms large cube crystal during its recrystallization, while aromatic domains of petroleum asphalt segregate from KCl crystals and nucleates on the surface of KCl microstructure. The pore size and morphologies can be easily adjusted by various KCl dosages. To our best knowledge, there is no report about the preparation of HPCs by liquid and solid template with in situ chemical activation for supercapacitors.

2. Experimental

2.1. Preparation of HPCs

Petroleum asphalt was obtained from Sinopec Group (7.1 wt % saturates, 24.9 wt % aromatics, 46.1 wt % resins and 18.0 wt % asphaltenes), the elemental analysis shows that petroleum asphalt has 89.3 wt % of carbon, 1.3 wt % of hydrogen, 1.7 wt % of sulfur, and 5.4 wt % of oxygen, 2.3 wt % of nitrogen. KCl was bought from Aladdin Ltd and KOH was purchased from Sinopharm Ltd. All other chemicals were of analytical grade and used without any further purification process. Typically, 2 g petroleum asphalt, 0–5.5 g potassium chloride and 6.5 g KOH were firstly grounded in an agate mortar for 20 min. Subsequently, the pulverized mixture was transferred into a corundum boat in a horizontal tube oven and heated to 800 °C at 5 °C min^{-1} and held at 800 °C for 120 min under N_2 atmosphere. Then, the remained impurities are highly reactive with water and can be easily removed by washing. Finally, HPCs were obtained after drying in an oven at 60 °C for 10 h. The prepared HPCs were named as $HPC_{X\text{-}Y}$, where X and Y represent the mass of petroleum asphalt and potassium chloride, respectively. Specifically, $HPC_{2\text{-}0}$ represents the control sample prepared by carbonizing the mixture of KOH and petroleum asphalt. The CPA was prepared by carbonizing the petroleum asphalt directly.

2.2. Characterization

The growth mechanism was researched by X-ray diffraction (XRD X'Pert PRO MPD, Holland). The morphologies and microstructures of the prepared HPCs were characterized by field emission scanning electron microscopy (SEM, Hitachi S-4800 Japan) and transmission electron microscopy (TEM, JEM-2100UHR, Japan). The defect level was conducted by Raman spectroscopy (Renishaw RM2000). The surface functional group was studied by X-ray photoelectron spectroscopy (XPS, Thermol Scientific Escalab 250XI). Thermogravimetry (TG) was recorded on Thermal Analyzer Shimadzu TA-60Ws with a heating rate of 10 °C min^{-1} from room temperature to 1000 °C in nitrogen atmosphere. Pore structure and specific surface area were determined by nitrogen adsorption–desorption isotherms on a sorptometer (Micromeritics, ASAP 2020, America), while the BET surface area was obtained by BET (Brunauer–Emmett–Teller) equation and the total pore volume (V_t) was obtained under a relative pressure (P/P_0) of 0.99. The micropore size distribution was estimated by the Horvanth–Kawazoe (HK) method and mesopore size distribution was calculated using the adsorption branch of the Barrett–Joyner–Halenda (BJH) method. The micropore volume (V_{mic}) was obtained using the t-plot method. The average pore diameter (D_{ap}) of HPCs was calculated by the equation of $D_{ap} = 4V_t/S_{BET}$.

2.3. Preparation and electrochemical measurements of HPCs electrodes

The carbon electrode was fabricated by mixing HPCs and polytetrafluoroethylene (PTFE) with a weight ratio of 9:1. Then, the mixture was rolled into thin film and further cut into round films (12 mm in diameter). Each round film with 2.5 mg cm^{-2} of mass loading was dried in vacuum oven at 120 °C for 2 h, and then pressed onto nickel foams to fabricate supercapacitors electrodes. Finally, the obtained electrodes were soaked it in 6 M KOH electrolyte under vacuum for 120 min. A button type supercapacitor was assembled by two similar electrodes and separated by a piece of polypropylene membrane. The cyclic voltammetry (CV) and electrochemical impedance spectroscopy (EIS) measurements were conducted on CHI760E electrochemical workstation (Chenhua, Shanghai, China). EIS was carried out over a frequency range of 100 KHz to 0.01 Hz with 5 mV ac amplitude. The galvanostatic charge-discharge (GCD) measurements and cycle life tests were conducted on a supercapacitance test system (SCTs, Arbin Instruments, USA). The specific capacitance of the working electrodes was calculated from the galvanostatic discharge process via the following equation:

$$C_{cell} = \frac{I\Delta t}{m\Delta V} \quad (1)$$

$$C_S = \frac{2I'\Delta t}{m'\Delta V} = \frac{4I\Delta t}{m\Delta V} \quad (2)$$

where C_{cell} (F g^{-1}) is the specific capacitances of the symmetric supercapacitor, C_s (F g^{-1}) is the single electrode capacitance, m' and I' (A) mean the mass of single electrode and the relevant current, I (A) stands for the discharge current, m (g) represents for the total mass of the active material in two-electrode cell, ΔV (V) and Δt (s) are the discharge voltage and the diacharge time in the discharge process.

The energy density (E, Wh kg^{-1}) and average power density (P,

W kg^{-1}) of the supercapacitors were calculated based on the following equations:

$$E = \frac{1}{2 \times 4 \times 3.6} C_s V^2 \quad (3)$$

$$P = \frac{E}{\Delta t} \quad (4)$$

Where V (V) represents the working voltage (excluding *IR* drop), t (h) stands for the discharge time.

3. Results and discussion

3.1. Formation of the porous carbon materials

Fig. 1 illustrates the overall synthetic schematic of porous carbon materials. During the synthesis process, petroleum asphalt (Asp) form liquid at around 150 °C, while KCl and KOH still maintain solid state. The viscous and liquid petroleum asphalt will uniformly coat on the surface of solid materials [29]. Fig. S1a shows the thermogravimetry curve of petroleum asphalt, the weight lost sharply at around 400 °C, which was owing to the gradually volatilization of light constituent and the polymerization of polycyclic aromatic hydrocarbons. After carbonization, the solid salt will be confined in the vacancy after the volatilization of light constituent which was confirmed by the TEM image of $HPC_{2\text{-}4.5}$ without removing KCl particles (highlighted by an orange square in Fig. S5c), where the cubic particles were confined by carbon layers. Then the chelation between metal ions and the functional groups of aromatic hydrocarbon directed the recrystallization process during the cooling process which contributed to the formation the 3D structure. Its growth rate can be controlled by varying the temperature and concentration [30]. To study the carbonization process and activation mechanism, Fig. S1b reveals the XRD patterns of $HPC_{2\text{-}4.5}$ at 400 °C, 600 °C and 800 °C without washing. The process could be divided into three steps. Firstly, apart from the KCl peaks (JCPDS card 41-1476), the peaks of K_2CO_3 can be observed at (JCPDS card 49-1093) around 400 °C, which was due to the reaction of KOH with petroleum asphalt to form K_2CO_3. Secondly, the diffraction peaks of K_2CO_3 were no longer visible and K_2O (JCPDS card 26-1327) could be detected at 600 °C. The detailed reaction was $K_2CO_3 \rightarrow K_2O + CO_2$ or $K_2CO_3 + C \rightarrow K_2O + 2\ CO$, indicating that the majority of the unstable K_2CO_3 has been transformed into K_2O. When the carbonization temperature rose up to 800 °C, K_2O was reduced by carbon and metallic potassium formed via the reaction of $K_2O + C \rightarrow 2\ K + CO$. Potassium vapors may intercalate between the carbon layers, but the metallic potassium was active and instable [27], thus no metallic potassium peak was detected through XRD results. The detailed possible activated mechanism was displayed in Fig. S2d, Fig. S1c shows the XRD patterns of $HPC_{2\text{-}4.5}$ before and after washing, the dash area shows the weak and broad peaks around 24° corresponding to the 002 plane of graphite. To further demonstrate that KCl particles only served as the self-assembly templates and porogen, the activate mechanism in absence of KCl was conducted and displayed in Fig. S2a, which was consistent with above mechanism. After washing by distilled water, pure hierarchical porous carbon with large surface area and ultrathin structure were easily obtained.

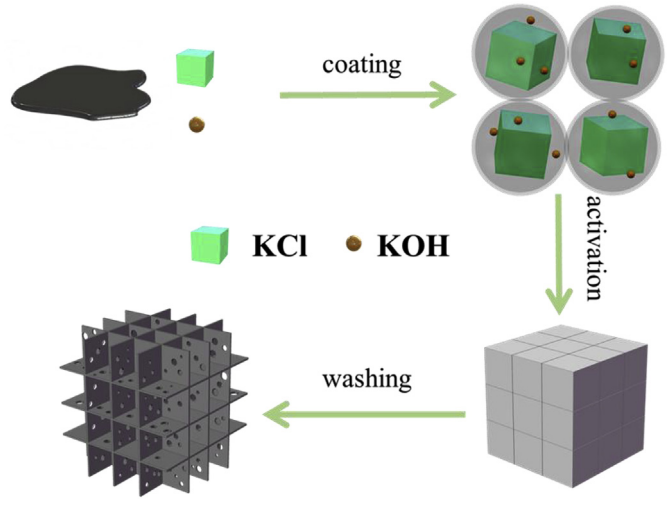

Fig. 1. Preparation schematic of HPCs. (A colour version of this figure can be viewed online.)

3.2. Structural characteristics and chemical properties of HPCs

Microscopic morphologies and pore texture of materials are vital to electrochemical performances. Fig. 2 shows the scanning electron microscopy (SEM) images of HPCs. As revealed by SEM images, the HPCs show porous and rough surface structure. Fig. 2a depicts the SEM image of CPA, no obvious pores and thicker block can be found. Compared with $HPC_{2\text{-}3.5}$ (in the Fig. 2b), $HPC_{2\text{-}4.5}$ shows uniform pore distribution and developed pore structure, which is favorable to the transport of electrolyte ions, resulting in high rate performance of HPCs. Fig. S5a shows the SEM image of $HPC_{2\text{-}0}$, it displays no significant change compared with other samples. Nevertheless, $HPC_{2\text{-}5.5}$ is mainly composed of macropores, the detail pore parameter is detected by N_2 adsorption-desorption isotherms. To further explain the effect of KCl dosages, Fig. 3a shows the TEM image of KCl, revealing its square like morphology with size around 50 nm [31,32]. TEM image of CPA is shown in Fig. 3b, the dark and sheet like structure reveal its thicker and undeveloped pore structure, corresponding to the SEM results. In addition, part of bright spot is due to the light constituent volatilization thus leaving the vacancy. The sheet-like structure of $HPC_{2\text{-}0}$ is shown in Fig. S5b, compared with the CPA image, $HPC_{2\text{-}0}$ displays transparent under irradiation of electron beam, reflecting its porous features. $HPC_{2\text{-}3.5}$ shows numerous approximate cages like structure and the diameter is around 300 nm, which is due to that KCl is wrapped by carbon layer during carbonization and serves as effective separator for aromatic domains of petroleum asphalt. After washing by distilled water, the pore structures remain unchanged. To demonstrate the role of KCl, the KCl dosage was increased and the amount of KOH maintained consistent. $HPC_{2\text{-}4.5}$ reveals ultrathin and homogeneous cage like porous morphologies, the circle diameter obviously increases to around 1 μm. The detailed morphology is displayed in Fig. S4a, the ultrathin structure expose abundant active sites for the adsorption of electrolyte ions. To better illustrate the homogeneous cage like porous morphology, the SEM images of $HPC_{2\text{-}4.5}$ were added and shown in Fig. S4b. Fig. 3e displays the wall thickness of cage like porous carbon about 20 nm, which serves as the ion-buffering reservoir and facilitates the rapid transport of electrolyte ions. $HPC_{2\text{-}5.5}$ shows the broken structure (Fig. 4f), which is due to the reason that excessive potassium chloride recrystallizes and immoderately grows into large crystal, thus inoperative effectively being wrapped by carbon layer when it recrystallizes [33]. The comparison of TEM morphologies between HPCs and $HPC_{2\text{-}0}$ further demonstrates that the homogeneous cage-like morphology is the inner structure of large KCl crystal. Notably, the TEM morphologies of HPCs are different, demonstrating that the geometry of KCl clusters nucleating from the vapour phase is controlled by coulomb interactions and the subcritical clusters tend

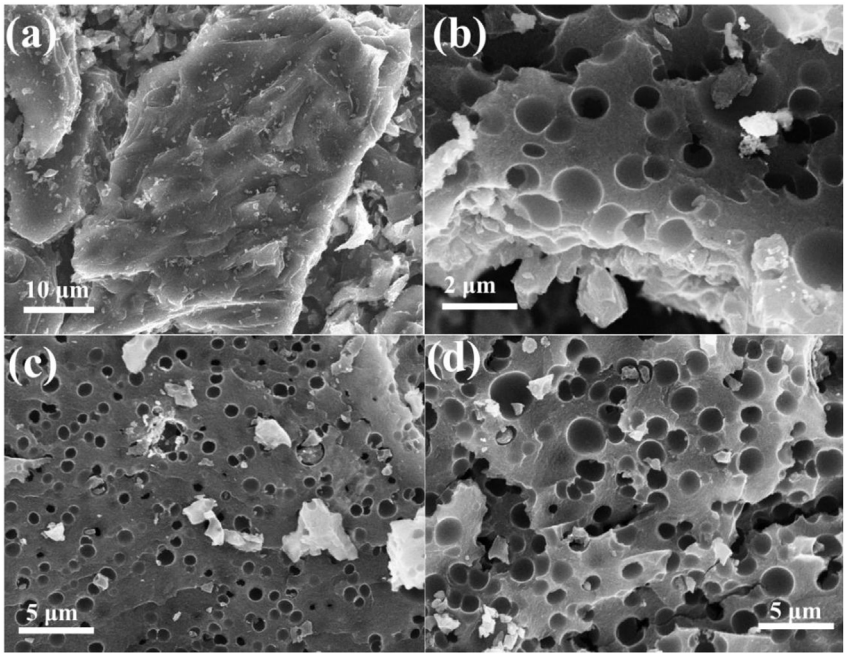

Fig. 2. (a) SEM image of CPA (b) SEM image of the $HPC_{2\text{-}3.5}$ (c) SEM image of the $HPC_{2\text{-}4.5}$ (d) SEM image of the $HPC_{2\text{-}5.5}$.

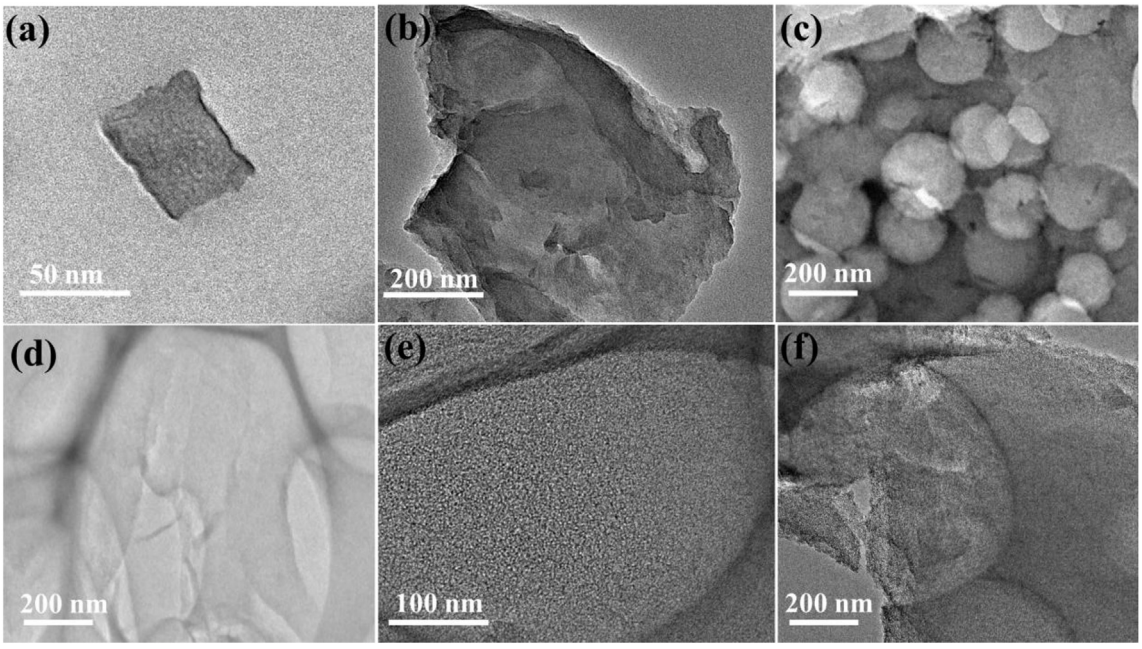

Fig. 3. TEM images of (a) KCl, (b) CPA, (c) $HPC_{2\text{-}3.5}$, (d) $HPC_{2\text{-}4.5}$ (e) HRTEM image of $HPC_{2\text{-}4.5}$, and (f) $HPC_{2\text{-}5.5}$.

to form spherical or cubic shape [34]. Therefore, the porous carbon structure can be easily tuned by adjusting the amount of KCl.

The pore properties of the HPCs were studied by N_2 adsorption-desorption isotherms. As shown in Fig. 4a, all curves of HPCs display type I isotherm based on the IUPAC classification, revealing the presence of a large number of micropores. At medium pressure, the small hysteresis loop in the isotherms of HPCs reveals the presence of mesopores. Hierarchical porous structure can not only offer abundant adsorption sites, but also reduce ion diffusion resistance. The pore structure parameters of the HPCs samples are summarized in Table 1. Remarkably, the specific surface area gradually decreases with the increase of KCl dosage. As we all know, both KOH and KCl can serve as activation agents for etching carbon skeleton. When both of them are employed, more carbon atoms will be etched away and the micropore will decrease along with the reducing of specific surface areas. Fig. 4b displays the pore size distribution of HPCs, the pore size distribution centers at 0.6–1 electrochemical active sites could significantly improve the capacitive behaviors [35]. The surface functional groups of HPCs are vital to electrochemical performance [36], thus XPS patterns of HPCs are given in Fig. 4c where three peaks corresponding to C1s, N1s and O1s can be observed. The detailed contents are listed in

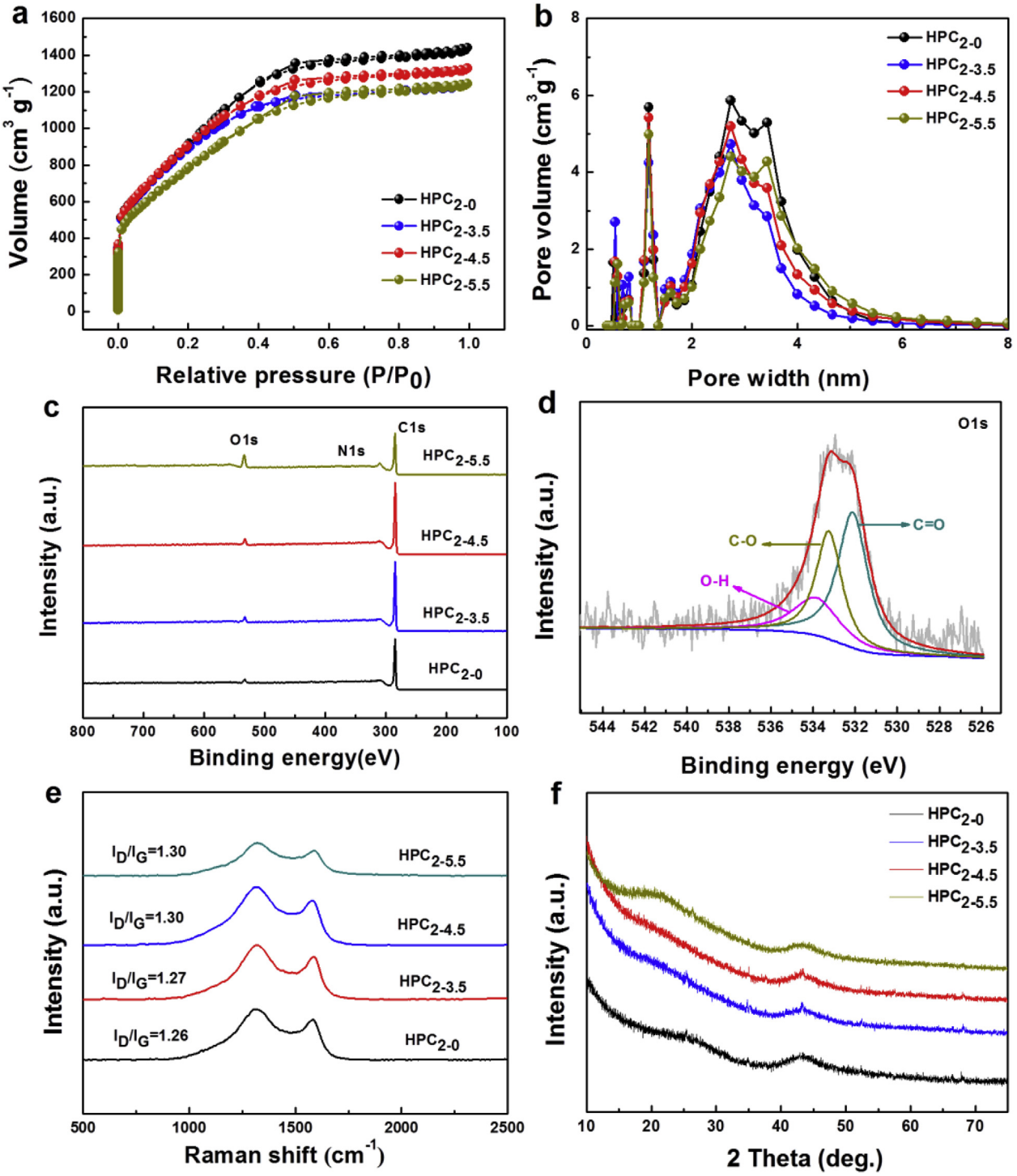

Fig. 4. (a) N_2 adsorption-desorption isotherms of the HPCs (b) Pore size distributions (c) Full XPS spectra of HPCs (d) O1s spectrum of $HPC_{2\text{-}4.5}$ (e) Raman spectra of HPCs (f) XRD patterns of the HPCs. (A colour version of this figure can be viewed online.)

Table S1 (Supplementary materials). It is noteworthy that the incorporation of heteroatoms into carbon structures is useful to improve the electrical properties by introducing pseudocapacitance and increasing wettability. Nitrogen doping can endow the inert graphene-like layered carbon with more electrochemical active sites [37]. The oxygen contents are different among HPCs and $HPC_{2\text{-}4.5}$ shows the maximum oxygen content. The oxygen functional groups could not only reduce internal resistance by increasing the hydrophilicity in aqueous electrolytes, but also fortify the capacitance by introducing the pseudocapacitance. The high-resolution O1s spectra of $HPC_{2\text{-}4.5}$ (525–545 eV) are presented in Fig. 4d where different types of O-containing groups could be verified on the surface of the prepared carbons, including C=O (531.9 eV), O-H (534.0 eV) and C–O (533.4 eV). Raman spectra (Fig. 4e) show the D bands at ~1320 cm^{-1} and G bands at ~1590 cm^{-1}, corresponding to the reflections of disordered and

Table 1
The pore structure parameters of HPCs.

Samples	D_{ap} nm	S_{BET} m^2 g^{-1}	S_{mic} m^2 g^{-1}	V_t cm^3 g^{-1}	V_{mic} cm^3 g^{-1}	V_{mic}/V_t %
$HPC_{2\text{-}0}$	2.89	3581	3425	2.20	1.99	90.4
$HPC_{2\text{-}3.5}$	2.66	3438	3328	2.03	1.84	90.6
$HPC_{2\text{-}4.5}$	2.65	3343	3219	1.90	1.74	91.6
$HPC_{2\text{-}5.5}$	3.02	2962	2775	1.90	1.67	87.9

nm and 2–4.0 nm. As reported in previous literature, the micropores dramatically increase the capacitance performances and the mesopores could effective increase the rate performance. The ultrahigh surface area for sufficient.

graphitic carbon, respectively. The high value of I_D/I_G (above 1.26) further reveals the amorphous nature of HPCs materials compared with that of carbon nanotubes and graphene [38,39]. As shown in Fig. 4e, the value of I_D/I_G increases by adding the KCl dosage, demonstrating that KCl acts as the self-assembly template as well as the porogen. Fig. 4f displays the XRD patterns of the HPCs, two weak and broad peaks at 23.4° and 43.5° correspond to the 002 and 101 planes of graphite, revealing the amorphous characteristics by KOH activation. A slightly sharp peak could be observed in XRD pattern of $HPC_{2\text{-}3.5}$ and $HPC_{2\text{-}4.5}$, which may be associated with increased graphitization [40]. As the amount KCl increases, the carbon produced under such a condition maybe over-activated. As a result, the peak has disappeared in the XRD pattern of $HPC_{2\text{-}5.5}$.

3.3. Electrochemical performances of HPCs

CV tests were carried out to evaluate the capacitive of HPCs. Fig. 5a displays the CV curves of four samples at the same scan rates of 2 mV s^{-1}. Obviously, all the curves display approximately rectangular shapes without distinct redox peaks, which demonstrates the ideal electrical double-layer capacitance (EDLC) behavior [41]. Remarkably, it is well known that the integral area corresponds to the capacitance of supercapacitors. Therefore, $HPC_{2\text{-}4.5}$ shows the maximum capacitance at the scan rate of 2 mV s^{-1}. To further detect the rate performances of $HPC_{2\text{-}4.5}$, the curves tested at scan rates range from 5 to 200 mV s^{-1} are displayed in Fig. 5b. It can be seen that even at a high scan rate of 200 mV s^{-1}, the curves still remain perfect rectangular shape, indicating the pure EDLC behavior and the rapid formation of the double-layer. In addition to the CV tests, GCD tests are employed to analyze the capacitive behavior of HPCs and shown in Fig. 5c. The GCD curves of $HPC_{2\text{-}4.5}$ reveal the isosceles triangle with minimum IR drop of 0.003 V at 0.1 A g^{-1}, demonstrating that the $HPC_{2\text{-}4.5}$ has lower internal resistance. The excellent electrochemical performance is due to the higher electronic conductivity and the existence of micropores (around 0.8–1 nm) and mesopores (2–4 nm). The micropores facilitate the capacitance performances of HPCs at different current densities while mesopores can act as fast ion-transportation channels to enhance ion diffusion kinetics in the carbon electrodes [42]. Furthermore, the specific capacitance of HPCs at different current density is revealed in Fig. 5d. The $HPC_{2\text{-}4.5}$ shows the highest capacitance of 277 F g^{-1} at 0.05 A g^{-1} and an excellent rate performance of 194 F g^{-1} at 20 A g^{-1}. Remarkably, the capacitance of $HPC_{2\text{-}4.5}$ is higher than that of $HPC_{2\text{-}3.5}$, which is due to the developed pore and ultrathin layer structure, exposing adsorption sites and reducing charge transfer resistance in 6 M KOH electrolyte. The size of hydrated K^+ ion is 0.36–0.42 nm while the hydrated OH^- ion existed as an $OH-(H_2O)_3$ complex is less than 0.50 nm [43]. In other words, the pore diameters with 0.6–1 nm could effectively contribute to the capacitance. $HPC_{2\text{-}4.5}$ possesses the largest miropores proportion. Thus, it has excellent capacitance performance. The capacitance performance of $HPC_{2\text{-}5.5}$ is deviant and inferior that of $HPC_{2\text{-}4.5}$, which are mainly associated with three factors. Firstly, $HPC_{2\text{-}5.5}$ has the lowest specific surface area and micropore volume, both of which play the vital role in capacitance of electrode materials. It is reported that microporous carbons with pores smaller than 1 nm are helpful to anomalously increase the capacitance [44]. Secondly, oxygen functional groups and nitrogen doping can store charges in a pseudocapacitance manner while the contents of oxygen and nitrogen in $HPC_{2\text{-}5.5}$ are the lowest among all these samples. Last but not least, the conductivity of $HPC_{2\text{-}5.5}$ is inferior to others' which is deteriorated to efficient charge transfer. To further explain the relationship between the property and materials, the impedance measurement was conducted and shown in Fig. 5e. The Nyquist plots consist of semicircles at high frequency region and vertical lines at low frequency range. Notably, $HPC_{2\text{-}4.5}$ exhibits the minimum resistance (shows in Fig. S2a). To quantitatively evaluate the electrode resistance, equivalent circuit model is introduced and displayed in Fig. 5f. In the equivalent circuit, the black represents the measured (Msd) plot and the red stands the calculated (Cad) plot, the Msd and Cad plots are nearly coincident, revealing this equivalent circuit model is suitable for this result. The calculated value of every circuit component is listed in Table S2, in which the Rs stands for the equivalent electrolyte resistance, Rct refers to the resistance involved in the adsorption/desorption of an electroactive species, Zw represents the Warburg resistance and CPE represents the constant phase element. Significantly, the value of Rs and Rct are 0.58 and 0.78 ohm, representing the electrode has excellent conductivity and less charge transfer resistance. To further explain the capacitance behavior, bode plot was introduced and shown in Fig. S2b, $HPC_{2\text{-}4.5}$ displays phase angle (−87.6°) and the smallest deviation to the ideal electric double layer capacitors (−90°), revealing the less pseudocapacitance behavior, which is corresponding to the CV results. To evaluate the cycle stability of $HPC_{2\text{-}4.5}$, a repetitive GCD test of button-type supercapacitor was conducted at the current density of 2 A g^{-1} over 10000 cycles (Fig. S2c). The capacitance maintains 95.1% of its initial value after 10000 cycles, demonstrating its good cycle stability. Fig. S2d shows the Ragone plots of HPCs at 6 M KOH electrolyte, $HPC_{2\text{-}4.5}$ displays the 9.1 Wh kg^{-1} at 26.2 W kg^{-1}, but this energy densities is far from meeting the requirements.

Fig. 6a shows the CV curves of as-fabricated symmetric supercapacitors at the same scan rates of 20 mV s^{-1} in 1 M Na_2SO_4 electrolyte with different voltage window. It can be obviously found that the CV curves remain rectangular shapes when the voltage is below 1.8 V, indicating ideal capacitive behavior and excellent reversibility. Remarkably, there is no significant increase of anodic current even at 1.8 V, which means that the electrolyte is not decomposed owing to the storage of nascent hydrogen on the HPCs below the thermodynamic potential for water decomposition [45]. After the voltage increases range to 2 V, the measured current density increases dramatically at the anode scan, which is on account of the decomposition of electrolyte into hydrogen and/or oxygen evolution. Thus, the optimal operating voltage range is 0–1.8 V. Apart from the CV curve, the GCD curves at different current densities show isosceles triangle while the IR drop with only 0.022 V at 0.5 A g^{-1} is displayed in the Fig. 6b, representing a low internal resistance and ideal electrochemical capacitive behavior.

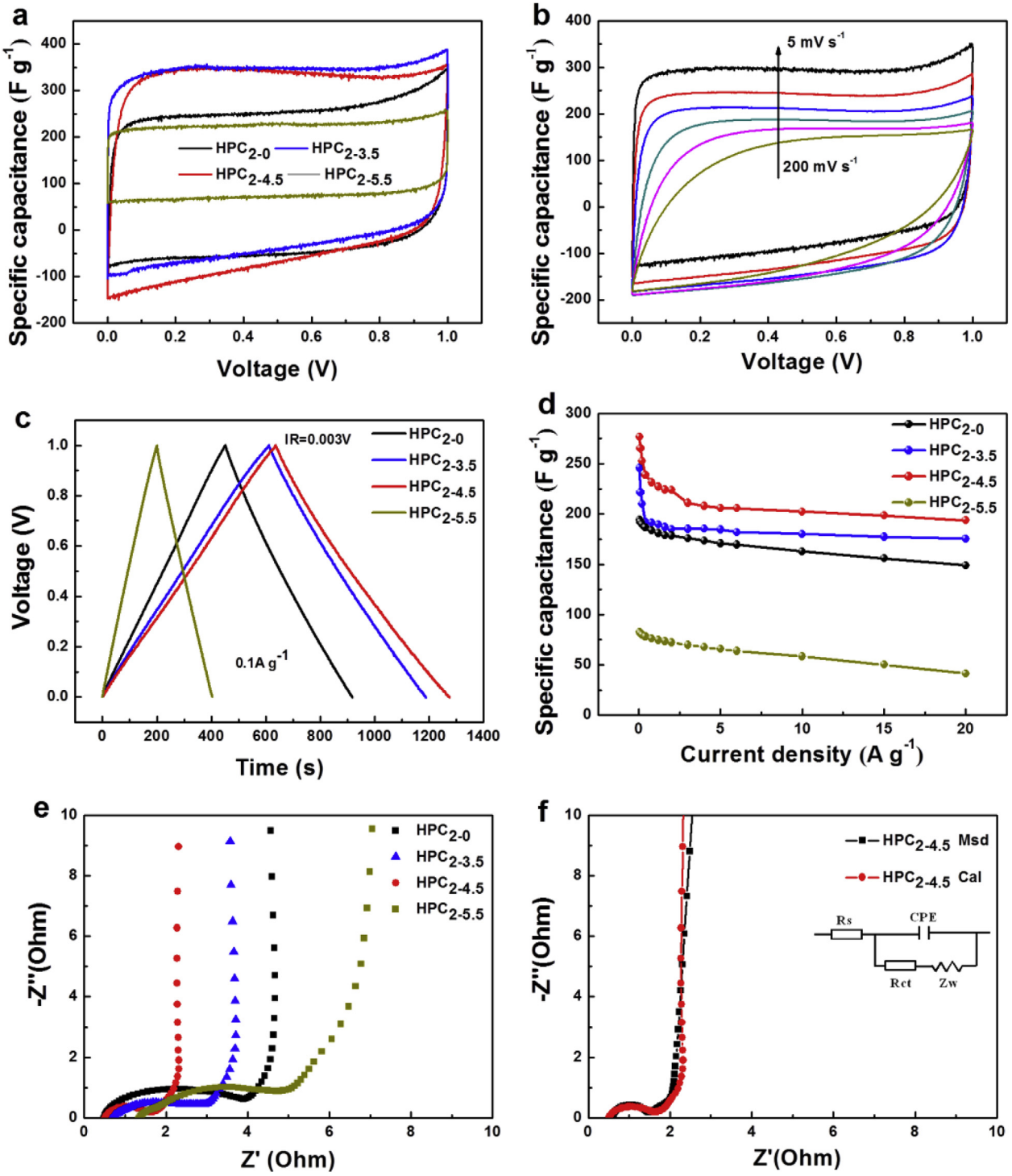

Fig. 5. (a) The CV curve of the HPCs at scan rate of 2 mV s^{-1} (b) The CV curve of $HPC_{2\text{-}4.5}$ at different scan rates (5, 10, 20, 50, 100, and 200 mV s^{-1}) (c) The GCD curve of the HPCs at 0.1 A g^{-1} (d) The capacitance performances of HPCs at different current densities (e) The Nquist plots of HPCs (f) Nyquist plot of $HPC_{2\text{-}4.5}$ (insert was the equivalent circuit model). (A colour version of this figure can be viewed online.)

The specific capacitance of $HPC_{2\text{-}4.5}$ at different current density is shown in Fig. 6c, it displays high specific capacitance up to 130 F g^{-1} at 0.05 A g^{-1} with 48% rate performance of 62 F g^{-1} at 20 A g^{-1}. The capacitance in 1 M Na_2SO_4 is less than in 6 M KOH electrolyte, which is because the size of SO_4^{2-} is 0.533 nm, much high than OH^- (0.36–0.42 nm). Although the specific capacitances in Na_2SO_4 electrolyte are obviously lower than that of KOH electrolytes, the $HPC_{2\text{-}4.5}$ delivers superior energy densities in Na_2SO_4 electrolyte due to the high work voltage (0–1.8 V). Fig. 6d shows the comparison of the energy densities at different aqueous electrolyte, the $HPC_{2\text{-}4.5}$ displays the energy densities of 14.2 Wh kg^{-1} at 444.5 W kg^{-1} in 1 M Na_2SO_4 aqueous electrolyte, nearly twice than

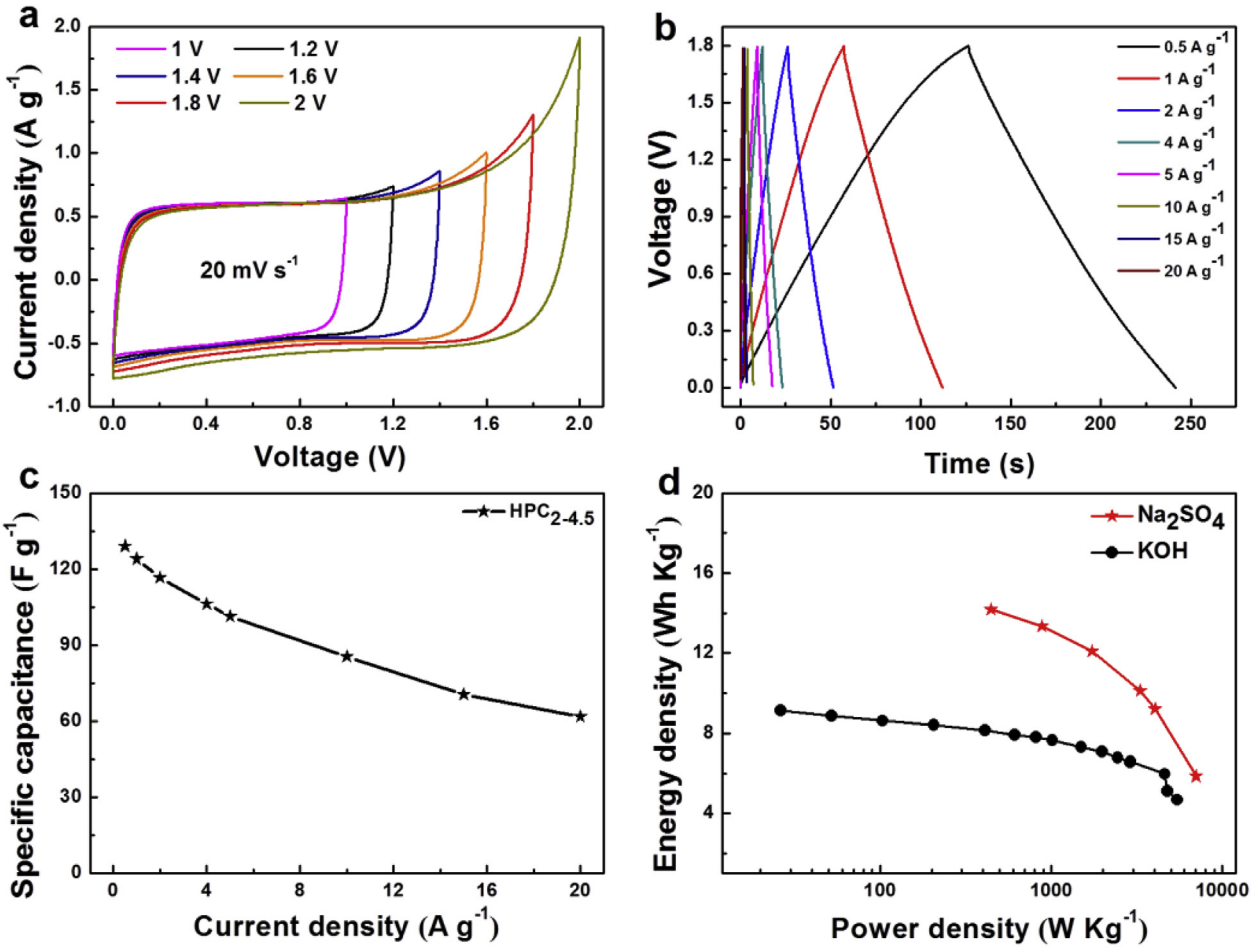

Fig. 6. (a) The CV curve of HPCs with scan rate of 20 mV s^{-1} with different voltage window at 1 M Na_2SO_4 (b) The GCD curves at different current densities (c) The specific capacitance of HPCs at different current densities (d) The Ragone plots of HPCs at different aqueous electrolyte. (A colour version of this figure can be viewed online.)

that in 6 M KOH. The energy density of our devices is higher than that of recently reported heteroatom-doped carbon-based symmetric supercapacitors (Table S3).

4. Conclusions

In summary, petroleum-asphalt-derived hierarchical porous carbon materials were synthesized by self-assembly template strategy assisted in-situ chemical activation. A synergistic effect of KCl and KOH activation was developed to prepare the ultrathin hierarchical porous carbon with ultrahigh specific surface area up to 3581 $m^2 g^{-1}$. The ultrathin and porous structure not only reduces the resistance by shortening the diffusion distance of electrolyte ions, but also serves as abundant porous channels and active sites for ion transport and storage. Notably, the mechanism of the formation and evolution of hierarchical pores is comprehensively researched. The as-assembled HPCs based symmetric supercapacitors exhibt high capacitance (277 F g^{-1} at 0.05 A g^{-1} in 6 M KOH), good rate performance (194 F g^{-1} at 20 A g^{-1}) and superior cycle stability (95.1% after 10000 charge discharge cycle at 2 A g^{-1}), delivering a high specific energy of 14.2 W h kg^{-1} at the specific power density of 445 W kg^{-1} with a wide operating voltage of 1.8 V in the aqueous Na_2SO_4 electrolyte. A new and facile strategy was presented to realize the high value utilization of petroleum asphalt, which holds great potential for scalable industrial manufacture.

Acknowledgments

This work was supported by the National Natural Science Foundation of China (Nos. 51372277, 51572296, U1662113); The Fundamental Research Funds for the Central Universities (15CX08005A). The Financial Support from Taishan Scholar Project, Scientific Research and Technology Development Project of Petrochina Co., LTD (2016B-2004(GF))

Appendix A. Supplementary data

Supplementary data related to this article can be found at https://doi.org/10.1016/j.carbon.2018.04.008.

References

[1] Z. Wu, L. Li, J.M. Yan, X.-B. Zhang, Materials design and system construction for conventional and new-concept supercapacitors, Adv. Sci. (2017) 1600382.
[2] C.Z. Yuan, B. Gao, L.F. Shen, S.D. Yang, L. Hao, X.J. Lu, F. Zhang, L.J. Zhang, X.G. Zhang, Hierarchically structured carbon-based composites: design, synthesis and their application in electrochemical capacitors, Nanoscale 3 (2011) 529–545.
[3] M. Chen, Y. Zhang, L. Xing, Y. Liao, Y. Qiu, S. Yang, W. Li, Morphology-conserved transformations of metal-based precursors to hierarchically porous micro-/nanostructures for electrochemical energy conversion and storage, Adv. Mater. 29 (2017) 1607015.
[4] Y.B. Tan, J.M. Lee, Graphene for supercapacitor applications, J. Mater. Chem. 1 (2013) 14814.
[5] Y. Zhang, X. Liu, S. Wang, L. Li, S. Dou, Bio-nanotechnology in high-performance supercapacitors, Adv. Energy Mater 7 (2017) 1700592.

[6] X. Zang, C. Shen, E. Kao, R. Warren, R. Zhang, K.S. Teh, J. Zhong, M. Wei, B. Li, Y. Chu, M. Sanghadasa, A. Schwartzberg, L. Lin, Titanium disulfide coated carbon nanotube hybrid electrodes enable high energy density symmetric pseudocapacitors, Adv. Mater. (2017) 1704754.
[7] S. Li, C. Yu, J. Yang, C. Zhao, M. Zhang, H. Huang, Z. Liu, W. Guo, J. Qiu, Superhydrophilic "nanoglue" stabilizing the metal hydroxides onto carbon materials for high-energy and ultralong-life asymmetric supercapacitors, Energy Environ. Sci. 10 (2017) 1958.
[8] Z. Ling, Z. Wang, M. Zhang, C. Yu, G. Wang, Y. Dong, S. Liu, Y. Wang, J. Qiu, Sustainable synthesis and assembly of biomass-derived B/N co-doped carbon nanosheets with ultrahigh aspect ratio for high-performance supercapacitors, Adv. Funct. Mater. 26 (2016) 111–119.
[9] Z. She, D. Ghosh, M.A. Pope, Decorating graphene oxide with ionic liquid nanodroplets: an approach leading to energy-dense, high-voltage supercapacitors, ACS Nano 11 (2017) 10077–10087.
[10] C. Wang, Y. Xiong, H. Wang, C. Jin, Q. Sun, Naturally three-dimensional laminated porous carbon network structured short nano-chains bridging nanospheres for energy storage, J. Mater. Chem. 5 (2017) 15759–15770.
[11] H. Wang, C. Wang, Y. Xiong, C. Jin, Q. Sun, Simple Synthesis of N-doped interconnected porous carbon from Chinese Tofu for high-performance supercapacitor and lithium-ion battery applications, J. Electrochem. Soc. 164 (2017) A3832–A3839.
[12] J. Zhu, K. Sakaushi, G. Clavel, M. Shalom, M. Antonietti, T.P. Fellinger, A general salt-templating method to fabricate vertically aligned graphitic carbon nanosheets and their metal carbide hybrids for superior lithium ion batteries and water splitting, J. Chem. Soc. 137 (2015) 5480–5485.
[13] Y. Liu, J. Goebl, Y. Yin, Templated synthesis of nanostructured materials, Chem. Soc. Rev. 42 (2013) 2610–2653.
[14] X. He, X. Li, H. Ma, J. Han, H. Zhang, C. Yu, N. Xiao, J. Qiu, ZnO template strategy for the synthesis of 3D interconnected graphene nanocapsules from coal tar pitch as supercapacitor electrode materials, J. Power Sources 340 (2017) 183–191.
[15] Y. Bu, T. Sun, Y. Cai, L. Du, O. Zhuo, L. Yang, Q. Wu, X. Wang, Z. Hu, Compressing carbon nanocages by capillarity for optimizing porous structures toward ultrahigh-volumetric-performance supercapacitors, Adv. Mater. 29 (2017) 1700470.
[16] H. Nishihara, T. Kyotani, Templated nanocarbons for energy storage, Adv. Mater. 24 (2012) 4473–4498.
[17] S. Marchesini, C.M. McGilvery, J. Bailey, C. Petit, Template-free synthesis of highly porous boron nitride: insights into pore network design and impact on gas sorption, ACS Nano 11 (2017) 10003–10011.
[18] J. Shao, F. Ma, G. Wu, C. Dai, W. Geng, S. Song, J. Wan, In-situ MgO ($CaCO_3$) templating coupled with KOH activation strategy for high yield preparation of various porous carbons as supercapacitor electrode materials, Chem. Eur J. 321 (2017) 301–313.
[19] X. Deng, B. Zhao, L. Zhu, Z. Shao, Molten salt synthesis of nitrogen-doped carbon with hierarchical pore structures for use as high-performance electrodes in supercapacitors, Carbon 93 (2015) 48–58.
[20] J. Qin, C.N. He, N.Q. Zhao, Z.Y. Wang, C.S. Shi, E.Z. Liu, J.J. Li, Graphene networks anchored with Sn@graphene as lithium ion battery anode, ACS Nano 8 (2014) 1728–1738.
[21] T.Y. Ma, Y. Zheng, S. Dai, M. Jaroniec, S.Z. Qiao, Mesoporous $MnCo_2O_4$ with abundant oxygen vacancy defects as high-performance oxygen reduction catalysts, J. Mater. Chem. 2 (2014) 8676–8682.
[22] F. Pan, A. Liang, Y. Duan, Q. Liu, J. Zhang, Y. Li, Self-growth-templating synthesis of 3D N, P,Co-doped mesoporous carbon frameworks for efficient bifunctional oxygen and carbon dioxide electroreduction, J. Mater. Chem. 5 (2017) 13104–13111.
[23] N. Fechler, T.P. Fellinger, M. Antonietti, A simple and sustainable pathway toward highly porous functional carbons from ionic liquids, Adv. Mater. 25 (2013) 75–79.
[24] X. Liu, C. Giordano, M. Antonietti, A facile molten-salt route to graphene synthesis, Small 10 (2014) 193–200.
[25] A.M. Abdelkader, Electrochemical synthesis of highly corrugated graphene sheets for high performance supercapacitors, J. Mater. Chem. 3 (2015) 8519–8525.
[26] X. Xie, X. He, X. Shao, S. Dong, N. Xiao, J. Qiu, Synthesis of layered microporous carbons from coal tar by directing, space-confinement and self-sacrificed template strategy for supercapacitors, Electrochim. Acta 246 (2017) 634–642.
[27] J. Zhou, Z. Li, W. Xing, H. Shen, X. Bi, T. Zhu, Z. Qiu, S. Zhuo, A New Approach to Tuning Carbon Ultramicropore Size at sub-angstrom level for maximizing specific capacitance and CO_2 uptake, Adv. Funct. Mater. 26 (2016) 7955–7964.
[28] Y. Li, D. Li, Y. Rao, X. Zhao, M. Wu, Superior CO_2, CH_4, andH_2 uptakes over ultrahigh-surface-area carbon spheres prepared from sustainable biomass-derived char by CO_2 activation, Carbon 105 (2016) 454–462.
[29] T.T. Guan, K.X. Li, J.H. Zhao, R.J. Zhao, G.L. Zhang, D.D. Zhang, J.L. Wang, Template-free preparation of layer-stacked hierarchical porous carbons from coal tar pitch for high performance all-solid-state supercapacitors, J. Mater. Chem. 5 (2017) 15869–15878.
[30] Y. Huang, J. Ge, J. Hu, J. Zhang, J. Hao, Y. Wei, Nitrogen-doped porous molybdenum carbide and phosphide hybrids on a carbon matrix as highly effective electrocatalysts for the hydrogen evolution reaction, Adv. Energy Mater. (2017) 1701601.
[31] J.W. Zhou, J. Qin, X. Zhang, C.S. Shi, E.Z. Liu, J.J. Li, N.Q. Zhao, C.N. He, 2D space-confined synthesis of few-layer MoS_2 anchored on carbon nanosheet for lithium-ion battery anode, ACS Nano 9 (2015) 3837–3848.
[32] T. Meng, L. Zheng, J. Qin, D. Zhao, M. Cao, A three-dimensional hierarchically porous Mo_2C architecture: salt-template synthesis of a robust electrocatalyst and anode material towards the hydrogen evolution reaction and lithium storage, J. Mater. Chem. 5 (2017) 20228–20238.
[33] J. Pampel, T.-P. Fellinger, Opening of bottleneck pores for the improvement of nitrogen doped carbon electrocatalyst, Adv. Energy Mater. 6 (2016) 1502389.
[34] W. Polak, K. Sangwal, Study of the geometry of KCl clusters nucleating from vapour and in aqueous solutions, J. Cryst. Growth 203 (1999) 434–442.
[35] J. Huang, Y. Liang, H. Hu, S. Liu, Y. Cai, H. Dong, M. Zheng, Y. Xiao, Y. Liu, Ultrahigh-surface-area hierarchical porous carbon from chitosan: acetic acid mediated efficient synthesis and its application in superior supercapacitors, J. Mater. Chem. 5 (2017) 24775–24781.
[36] D. Hulicova-Jurcakova, M. Seredych, G.Q. Lu, T.J. Bandosz, Combined effect of nitrogen- and oxygen-containing functional groups of microporous activated carbon on its electrochemical performance in supercapacitors, Adv. Funct. Mater. 19 (2009) 438–447.
[37] T. Lin, I.-W. Chen, F. Liu, C. Yang, H. Bi, F. Xu, et al., Nitrogen-doped mesoporous carbon of extraordinary capacitance for electrochemical energy storage, Science 350 (2015) 1508–1513.
[38] C. Li, X. Zhang, K. Wang, X. Sun, G. Liu, J. Li, H. Tian, J. Li, Y. Ma, Scalable self-propagating high-temperature synthesis of graphene for supercapacitors with superior power density and cyclic stability, Adv. Mater. 29 (2017) 1604690.
[39] N.I.T. Ramli, S. Abdul Rashid, Y. Sulaiman, M.S. Mamat, S.A. Mohd Zobir, S. Krishnan, Physicochemical and electrochemical properties of carbon nanotube/graphite nanofiber hybrid nanocomposites for supercapacitor, J. Power Sources 328 (2016) 195–202.
[40] Y. Gong, D. Li, C. Luo, Q. Fu, C. Pan, Highly porous graphitic biomass carbon as advanced electrode materials for supercapacitors, Green Chem. 19 (2017) 4132–4140.
[41] N. Choudhary, C. Li, J. Moore, N. Nagaiah, L. Zhai, Y. Jung, J. Thomas, Asymmetric supercapacitor electrodes and devices, Adv. Mater. 29 (2017) 1605336.
[42] S. Kondrat, C.R. Pérez, V. Presser, Y. Gogotsi, A.A. Kornyshev, Effect of pore size and its dispersity on the energy storage in nanoporous supercapacitors, Energy Environ. Sci. 5 (2012) 6474.
[43] W.H. Choi, M.J. Choi, J.H. Bang, Nitrogen-doped carbon nanocoil array integrated on carbon nanofiber paper for supercapacitor Electrodes, ACS Appl. Mater. Interfaces 7 (2015) 19370–19381.
[44] R. Lin, P.L. Taberna, J. Chmiola, D. Guay, Y. Gogotsi, P. Simon, Microelectrode study of pore size, ion size, and solvent effects on the charge/discharge behavior of microporous carbons for electrical double-layer capacitors, J. Electrochem. Soc. 156 (2009) A7.
[45] H. Peng, G. Ma, K. Sun, Z. Zhang, Q. Yang, Z. Lei, Nitrogen-doped interconnected carbon nanosheets from pomelo mesocarps for high performance supercapacitors, Electrochim. Acta 190 (2016) 862–871.